



Delft University of Technology

## A simple finite-difference scheme for handling topography with the first-order wave equation

Mulder, Wim; Huiskes, M.J.

**DOI**

[10.1093/gji/ggx178](https://doi.org/10.1093/gji/ggx178)

**Publication date**

2017

**Document Version**

Final published version

**Published in**

Geophysical Journal International

**Citation (APA)**

Mulder, W., & Huiskes, M. J. (2017). A simple finite-difference scheme for handling topography with the first-order wave equation. *Geophysical Journal International*, 210(1), 482-499. <https://doi.org/10.1093/gji/ggx178>

**Important note**

To cite this publication, please use the final published version (if applicable). Please check the document version above.

**Copyright**

Other than for strictly personal use, it is not permitted to download, forward or distribute the text or part of it, without the consent of the author(s) and/or copyright holder(s), unless the work is under an open content license such as Creative Commons.

**Takedown policy**

Please contact us and provide details if you believe this document breaches copyrights. We will remove access to the work immediately and investigate your claim.

# A simple finite-difference scheme for handling topography with the first-order wave equation

W.A. Mulder<sup>1,2</sup> and M.J. Huiskes<sup>1</sup>

<sup>1</sup>Shell Global Solutions International B.V., Amsterdam, The Netherlands

<sup>2</sup>Delft University of Technology, Delft, The Netherlands. E-mail: [W.A.Mulder@tudelft.nl](mailto:W.A.Mulder@tudelft.nl)

Accepted 2017 April 28. Received 2017 April 26; in original form 2016 October 24

## SUMMARY

One approach to incorporate topography in seismic finite-difference codes is a local modification of the difference operators near the free surface. An earlier paper described an approach for modelling irregular boundaries in a constant-density acoustic finite-difference code, based on the second-order formulation of the wave equation that only involves the pressure. Here, a similar method is considered for the first-order formulation in terms of pressure and particle velocity, using a staggered finite-difference discretization both in space and in time. In one space dimension, the boundary conditions consist in imposing antisymmetry for the pressure and symmetry for particle velocity components. For the pressure, this means that the solution values as well as all even derivatives up to a certain order are zero on the boundary. For the particle velocity, all odd derivatives are zero. In 2D, the 1-D assumption is used along each coordinate direction, with antisymmetry for the pressure along the coordinate and symmetry for the particle velocity component parallel to that coordinate direction. Since the symmetry or antisymmetry should hold along the direction normal to the boundary rather than along the coordinate directions, this generates an additional numerical error on top of the time stepping errors and the errors due to the interior spatial discretization. Numerical experiments in 2D and 3D nevertheless produce acceptable results.

**Key words:** Numerical modelling; Computational seismology; Wave propagation.

## 1 INTRODUCTION

Numerical modelling of wave propagation in the presence of surface topography requires the incorporation of non-flat boundaries. Embedding irregular boundaries into a finite-difference method is an old problem (Shortley & Weller 1938). It can be avoided altogether with finite-element or finite-volume or mesh-free methods, but usually at a higher computational cost. Given the existing, highly optimized finite-difference code base, a local modification of finite-difference stencils close to the irregular boundary is more attractive.

An obvious approach for dealing with topography is the introduction of an air layer. The extreme density contrast may require some smoothing to preserve stability (Schultz 1997; Bartel *et al.* 2000; Haney 2007). The presence of an air wave can be suppressed by setting the sound speed in air equal to that at the surface, using constant extrapolation. There are several formulations of the vacuum approach (Boore 1972; Robertsson 1996; Mittet 2002; Bohlen & Saenger 2006; Moczo *et al.* 2007; Zeng *et al.* 2012). Numerical experiments with a higher-order finite-difference scheme show that the numerical error increases to only first order in space (Zhebel *et al.* 2014, a.o.).

In case of gentle and smooth topography, curvilinear coordinates that fit the boundary will provide accurate solutions (e.g. Tessmer & Kosloff 1994; Hestholm & Ruud 1998, 2002; Zhang & Chen 2006; De la Puente *et al.* 2014; Petersson & Sjögreen 2015; Solano *et al.* 2016), but at a higher computational cost. Finite elements (e.g. Seriani *et al.* 1992; Mulder 1996; Komatitsch & Vilotte 1998; Chin-Joe-Kong *et al.* 1999; Bécache *et al.* 2000; Cohen *et al.* 2001; Joly 2003; Rivière & Wheeler 2003; Grote *et al.* 2006; Dumbser *et al.* 2007; De Basabe & Sen 2007; Pelties *et al.* 2010; Etienne *et al.* 2010; Zhebel *et al.* 2011; Moczo *et al.* 2011; Minisini *et al.* 2013; Modave *et al.* 2015; Mulder & Shamasundar 2016) can deal with topography in a natural way, but require mesh generation, as do mimetic finite-difference (Lipnikov *et al.* 2014, for a review) and finite-volume methods (Dormy & Tarantola 1995; Zhang & Liu 1999; Benjema *et al.* 2007; Zhang & Gao 2009).

As already mentioned, locally adapted stencils may be a better choice. There are several examples in the literature, with various degrees of complexity and robustness (Strand 1994; Carpenter *et al.* 1999; Piraux & Lombard 2001; Mattsson & Nordström 2006; Lombard *et al.* 2008; Fornberg 2010; Seo & Mittal 2011; AlMuhaidib *et al.* 2011; Zhang *et al.* 2013; Neseemann 2014; Mattsson *et al.* 2014; Gao *et al.* 2015; Hu 2015).

An earlier paper described a simple scheme for the second-order formulation of the acoustic wave equation (Mulder 2017). It employs modified 1-D stencils, which decreases the accuracy but improves simplicity and stability. It was observed that points close to the zero-pressure boundary should be excluded from the scheme to avoid severe time step restrictions. Here, the alternative formulation of the wave equation as a first-order system is considered, as it is more suited for variable-density acoustics and potentially can be extended to the anisotropic acoustic case. The same approach of modified, locally 1-D stencils is followed. Also, the 1-D symmetry conditions are imposed. The pressure is antisymmetric with respect to the boundary in the normal direction. Not only its zeroth derivative—the solution itself—but also all even derivatives are prescribed to be zero on the boundary. For the particle velocities, symmetry is imposed, meaning that all odd derivatives up to a given order are set to zero. In the 2-D case, the 1-D assumption can still be used as an approximation. Antisymmetry for the pressure and symmetry for one of the particle velocity components is imposed along coordinate directions rather than the normal direction. This leads to an additional numerical error if the boundary does not coincide with the horizontal or vertical direction.

In Section 2, we describe the 1-D numerical scheme. Its stability is considered in Section 2.2. The 1-D stability is insufficient when going to more than one space dimension and we therefore examine the positivity of the product operator in Section 2.3. As it is known that cancellation of numerical errors may be lost on irregular grids, causing a decrease of accuracy, we examine the effect of the boundary on the spatial accuracy in Section 2.4. In Section 2.5, we consider a one-sided variant of the boundary scheme that does not employ zero higher derivatives on the boundary. In 1D, this scheme is only stable up to order 6. In 2-D, we were not able to stabilize it beyond order 4. Section 3 describes the extension of the 1-D scheme to 2D, using a locally 1-D approximation.

Section 4 contains results for a number of 2-D numerical experiments. We consider three problems with an exact solution, followed by one with a very rough surface and two problems with realistic topography. Section 5 describes a 3-D test with realistic topography and Section 6 summarizes the main conclusions.

## 2 1-D METHOD

### 2.1 Finite-difference discretization

The 1-D first-order formulation of the acoustic wave equation reads

$$\frac{1}{\rho c^2} \frac{\partial p}{\partial t} = \frac{\partial v}{\partial x} + f, \quad \rho \frac{\partial v}{\partial t} = \frac{\partial p}{\partial x}, \quad (1)$$

with pressure  $p(t, x)$ , particle velocity  $v(t, x)$ , sound speed  $c(x)$ , density  $\rho(x)$  and optional source term  $f(t, x)$ . Note that many authors replace  $p$  by  $-p$ . The source term is often of the form  $f(t, x) = w(t)\delta(x - x_s)$  for a source at  $x_s$  with wavelet  $w(t)$ .

With a staggered finite-difference discretization, the solution  $p_j^n$  at time  $t_n = t_0 + n\Delta t$  is represented on a grid  $x_j = x_0 + j\Delta x$ ,  $j = 0, 1, \dots, N_x - 1$ , whereas  $v_{j+1/2}^{n+1/2}$  is staggered in time and in space on  $x_{j+1/2} = x_0 + (j + \frac{1}{2})\Delta x$ ,  $j = 0, 1, \dots, N_x - 2$ .

A staggered discretization of eq. (1) is

$$\frac{p_j^{n+1} - p_j^n}{\Delta t} = \rho_j c_j^2 [(D^- v^{n+1/2})_j + f_j], \quad \frac{v_{j+1/2}^{n+1/2} - v_{j+1/2}^{n-1/2}}{\Delta t} = \rho_{j+1/2}^{-1} (D^+ p^n)_{j+1/2}. \quad (2)$$

The forward difference operator  $D^+$  of even order  $M$  takes points on the  $x_j$  grid to the  $x_{j+1/2}$  grid and is defined by

$$\Delta x (D^+ p)_{j+1/2} = \sum_{k=1}^{M/2} w_k (p_{j+k} - p_{j+1-k}), \quad (3)$$

where

$$w_k = \frac{(-1)^{k+1}}{(k - \frac{1}{2})^2} \frac{k + \frac{1}{2}M}{2^{2M}} \binom{M}{k + \frac{1}{2}M} \binom{M}{\frac{1}{2}M}, \quad k = 1, \dots, \frac{1}{2}M. \quad (4)$$

The backward difference operator  $D^- = -(D^+)^T$ , where  $(\cdot)^T$  denotes the transpose. For the 1-D example, zero Dirichlet boundary values are imposed for  $p$  and zero Neumann boundary values for  $v$ . In the standard case with boundaries on grid points, the left boundary is located at  $x = x_0$  and the right at  $x_{N_x - 1}$ . These boundary conditions can be implemented by imposing antisymmetry of  $p$  and symmetry of  $v$  across the boundary. Then,  $D^+$  maps a set of  $N_x$  points, including the zero values at the boundaries, to  $N_x - 1$  interior points. The operator  $D^-$  does the reverse.

An example for the lowest order,  $M = 2$ , and  $N_x = 5$  points is

$$D^+ = \frac{1}{\Delta x} \begin{pmatrix} 0 & 1 & 0 & 0 & 0 \\ 0 & -1 & 1 & 0 & 0 \\ 0 & 0 & -1 & 1 & 0 \\ 0 & 0 & 0 & -1 & 0 \end{pmatrix}, \quad D^- = -\frac{1}{\Delta x} (D^+)^T = \frac{1}{\Delta x} \begin{pmatrix} 0 & 0 & 0 & 0 \\ -1 & 1 & 0 & 0 \\ 0 & -1 & 1 & 0 \\ 0 & 0 & -1 & 1 \\ 0 & 0 & 0 & 0 \end{pmatrix}. \quad (5)$$

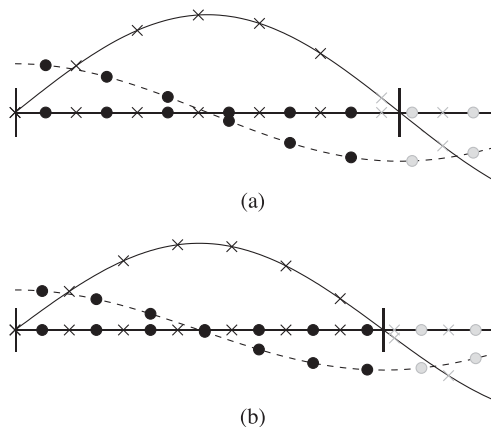


**Figure 1.** Staggered grid. The crosses mark the positions and values of the pressure variables,  $p_j$ , the dots those of the particle velocity,  $v_{j+1/2}$ . Vertical bars indicate the left and right boundary. The latter is positioned at a distance  $\xi \Delta x$  to the right of the rightmost interior pressure point. There are two cases, one with  $\xi < \frac{1}{2}$  (a), and one with  $\xi \geq \frac{1}{2}$  (b) allowing for an extra point for  $v_{j+1/2}$ . A few of the extrapolated points are shown in grey. In (a), the interior pressure value closest to the boundary has to be dropped from the discrete difference operator to obtain stability in the multidimensional case and is treated by 1-D polynomial extrapolation instead, just like the exterior points.

We immediately have that the second-order product operator  $B = -D^- D^+ = (D^+)^T D^+$  is symmetric and non-negative, which is an attractive property for obtaining time-stepping stability.

In the more general case, the right boundary is located at  $x_b = x_{N_x} - 1 + \xi \Delta x$  with  $\xi \in (0, 1]$ . We may also consider  $\xi > 1$  for the purpose of analysis. For now, the boundary on the left, at  $x_0$ , is assumed to coincide with a grid point. Depending on  $\xi$ , we have to consider two cases, sketched in Fig. 1. If  $\xi < \frac{1}{2}$ ,  $D^+$  maps a set of  $N_x$  points to  $N_x - 1$  and  $D^-$  does the reverse. For  $\xi \geq \frac{1}{2}$ , we may choose to let both  $D^+$  and  $D^-$  map  $N_x$  points to  $N_x$  points.

As in the second-order case (Mulder 2017), the discretization near the boundary can be derived as follows. We take a Taylor series expansion around the boundary, with prescribed zero even derivatives for  $p$  or zero odd derivatives for  $v$ . For a scheme of order  $M$ , a total of  $\frac{1}{2}M$  additional interior points near the boundary are needed to determine the remaining degrees of freedom of the polynomial that represents the truncated Taylor series. Next, the resulting polynomial is used for extrapolation to the first set of  $\frac{1}{2}M$  points in the exterior, just outside the boundary. Appendix A lists the extrapolation operators for orders  $M = 2-8$ . After extrapolation, we can apply the standard finite-difference weights to obtain expressions for the derivatives in the interior.

## 2.2 Stability

In 1D, a spatial scheme of even order  $M$  on an equidistant grid  $x_j = x_0 + j\Delta x$  has a staggered numerical first derivative

$$D^+ = \frac{1}{\Delta x} \sum_{k=1}^M w_k (T^{k-1/2} - T^{1/2-k}), \quad (6)$$

with a shift operator  $T$  defined by  $T^m u_j = u_{j+m}$  for a solution  $u_j$  that approximates  $u(x_j)$ . The weights are given in eq. (4). The Fourier symbol  $\hat{D}^+$  is obtained by replacing  $T$  with  $\exp(i\eta)$ , where  $\eta = k\Delta x$  for a wavenumber  $k$  and  $|\eta| \leq \pi$ . Then,

$$\hat{D}^+ = \frac{2i}{\Delta x} f_M(\zeta), \quad f_M(\zeta) = \sum_{k=0}^{M/2-1} c_k \zeta^{2k+1}, \quad (7a)$$

with

$$\zeta = \sin(\frac{1}{2}\eta), \quad c_k = \frac{1}{4^k(2k+1)} \binom{2k}{k}. \quad (7b)$$

Note that  $f_M(\zeta)$  is the truncated series of  $\arcsin(\zeta)$  around  $\zeta = 0$ . The coefficients  $c_k$  can be evaluated recursively by  $c_1 = 1$ ,  $c_2 = 1/6$ , and  $c_{k+1}/c_k = (2k-1)^2/(2k(2k+1))$ . Time-stepping stability for a standard leap-frog scheme involves

$$(\hat{g} - 1)\hat{p} = \Delta t \rho c^2 \hat{D}^- \hat{g}^{1/2} \hat{v}, \quad (\hat{g}^{1/2} - \hat{g}^{-1/2}) \hat{v} = \Delta t \rho^{-1} \hat{D}^+ \hat{p}, \quad (8)$$

where  $\hat{g} = \exp(-i\omega\Delta t)$  is the amplification factor after one time step at an angular frequency  $\omega$  and we have assumed constant material properties. After eliminating  $\hat{v}$  and defining  $B = -c^2 D^- D^+$  and  $\sigma = c\Delta t/\Delta x$ , we obtain

$$\hat{g} = 1 - \frac{1}{2}(\Delta t)^2 \hat{B} \pm i\sqrt{(\Delta t)^2 \hat{B}[1 - (\Delta t/2)^2 \hat{B}]}. \quad (9)$$

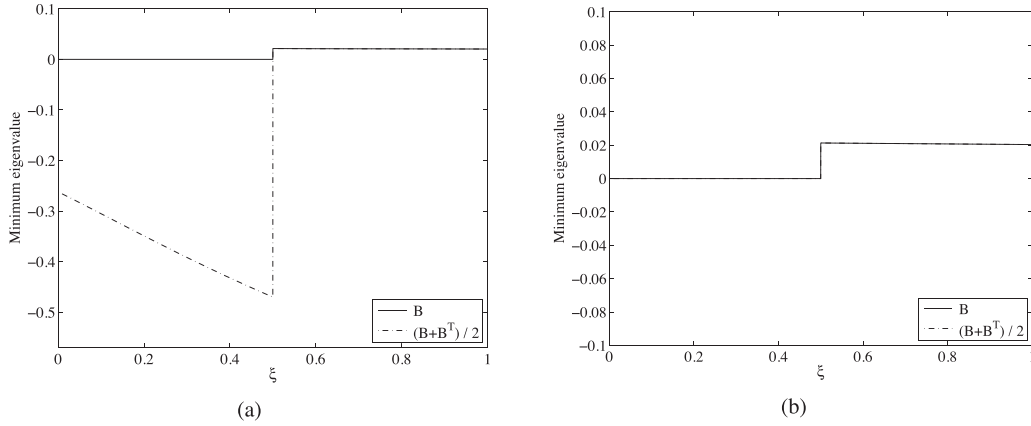


**Figure 2.** Minimum eigenvalue of  $B$  and  $B_{\text{sym}}$  as a function of  $\xi$  for  $M_d = M_n = 4$  if (a)  $\xi_{0,p} = 0$ , or (b)  $\xi_{0,p} = \frac{1}{2}$ , that is, pressure values closer to the Dirichlet boundary than half a grid spacing are ignored in the extrapolation. In the last panel, the curves lie on top of each other.

If  $0 \leq (\Delta t/2)^2 \hat{B} \leq 1$ , then  $|\hat{g}| = 1$ , implying energy conservation. From  $\hat{D}^- = -(\hat{D}^+)^* = \hat{D}^+$ , we obtain  $\hat{B} = [2cf_M(\xi)/\Delta x]^2$ , leading to the stability condition  $c\Delta t/\Delta x \leq 1/\max_{\xi \in [-1, 1]} f_M(\xi) \leq 1/f_M(1)$ . The upper bound decreases from 1 for  $M = 2$  to  $2/\pi = 0.64$  for  $M \rightarrow \infty$ . Note that the upper bound follows from the condition that the argument of the square-root in eq. (9) be non-negative. It also provides a lower bound requiring  $B$  to have non-negative eigenvalues. The above Von Neumann stability analysis (Charney *et al.* 1950; Haney 2007) is valid on a periodic grid.

With variable coefficients  $\rho(x)$  and  $c(x)$ , the time step  $\Delta t$  should be chosen such that the eigenvalues of the matrix  $B = -(\rho c^2 D^-)(\rho^{-1} D^+)$  lie between zero and  $(2/\Delta t)^2$ . For Dirichlet boundary conditions coinciding with grid points, we have  $\xi = 0$  and  $D^- = -(D^+)^T$ . Then, a similarity transform provides  $\hat{B} = (c\sqrt{\rho})^{-1} B (c\sqrt{\rho}) = (D^+ c\sqrt{\rho})^T (D^+ c\sqrt{\rho})$ , showing that the eigenvalues of  $B$  are real and non-negative.

For  $\xi > 0$ , the symmetry of  $B$  is already lost in the constant-coefficient case. In the numerical experiments of Sections 2.3 and 2.4, we computed the eigenvalues of  $B$  numerically and observed that they are real-valued, non-negative and that the largest one is slightly smaller than  $[2f_M(1)]^2$ . A complex pair of eigenvalues—or a  $2 \times 2$  Jordan block if one insists on staying with real values—would imply a growing mode causing instability.

In the second-order formulation, interior points too close to the boundary had to be dropped from the discretization to avoid a severe reduction of the maximum time step for decreasing  $\xi < \frac{1}{2}$  (Mulder 2017). In the first-order formulation considered here, this does not appear to be necessary in 1D. In more than one space dimension, however, the fact that the 1-D operator  $B$  has non-negative eigenvalues does not guarantee stability, as will be discussed next.

### 2.3 Positivity

The 1-D case is stable for all relative boundary positions  $\xi \in [0, 1]$ , but an instability shows up in the 2-D case. Here, we will examine its cause and potential remedies.

In the constant-coefficient case with  $c = 1$ , the 1-D product operator  $B = -c^2 D^- D^+$  has non-negative and bounded eigenvalues. The usual approach for estimating stability in 2D is the condition  $\Delta t \leq 2/\sqrt{\lambda_{\max}(B^x + B^z)}$ , where the spectral radius is estimated by using  $\lambda_{\max}(B^x + B^z) \leq \lambda_{\max}(B^x) + \lambda_{\max}(B^z)$ . This, however, implicitly assumes that both 1-D product operators  $B^x$  and  $B^z$  are non-negative matrices, which is not the same as them having non-negative eigenvalues. Unfortunately, the 1-D matrices are not non-negative: there exist vectors  $\mathbf{y}$  with  $\|\mathbf{y}\| = 1$  such that  $\mathbf{y}^T B \mathbf{y} < 0$ . An equivalent statement is that the matrix  $B_{\text{sym}} = \frac{1}{2}(B + B^T)$  has some negative eigenvalues. As a result, the sum of the matrices  $B^x$  for the  $x$ -direction and  $B^z$  for the  $z$ -direction is not guaranteed to have non-negative eigenvalues, even if  $B^x$  and  $B^z$  themselves have non-negative eigenvalues. This causes the 2-D scheme to be unstable. In eq. (9), the negative eigenvalues cause  $\hat{g}$  to be real-valued with one of the roots becoming larger than one, implying an unstable mode.

As an illustration, consider a domain  $[0, 1 + (\xi - 1)\Delta x]$ ,  $\xi \in [0, 1]$ , with grid spacing  $\Delta x = 1/(N_x - 1)$ , grid points for the pressure at  $x_{p,j} = j\Delta x$ ,  $j = 0, 1, \dots, N_x - 2$  and for the particle velocity at  $x_{v,j} = (j + \frac{1}{2})\Delta x$  with  $j = 0, 1, \dots, N_x - 3$  for  $\xi < \frac{1}{2}$  and  $j = 0, 1, \dots, N_x - 2$  if  $\xi \geq \frac{1}{2}$ . Fig. 2 plots the smallest eigenvalues for  $B$  and  $B_{\text{sym}}$  as a function of  $\xi$  for a scheme of order  $M = 4$ . Whereas  $B$  has only non-negative eigenvalues, that clearly is not true for  $B_{\text{sym}}$ .

We have considered two ways to solve this problem. One is to adopt a general form for  $D^+$  and  $D^-$  near the boundary and determine the coefficients by requiring that (i) the scheme is exact for polynomials up to degree  $M - 1$  that obey the (anti)symmetry condition at the boundary, and (ii) the matrix  $B = -D^- D^+$  is non-negative. The last condition can be verified by computing the eigenvalues of  $B_{\text{sym}}$  or by requiring the determinants of all principal minors to be non-negative.

We have attempted to tackle this problem with a symbolic algebra package and were able to obtain results by numerical optimization for  $M = 4$  on a grid with a small number of points. However, no closed-form solution could be derived for this order, let alone for the higher orders  $M = 6$  or  $M = 8$ . A simple alternative was found in the approach used in the preceding paper (Mulder 2017), where interior points

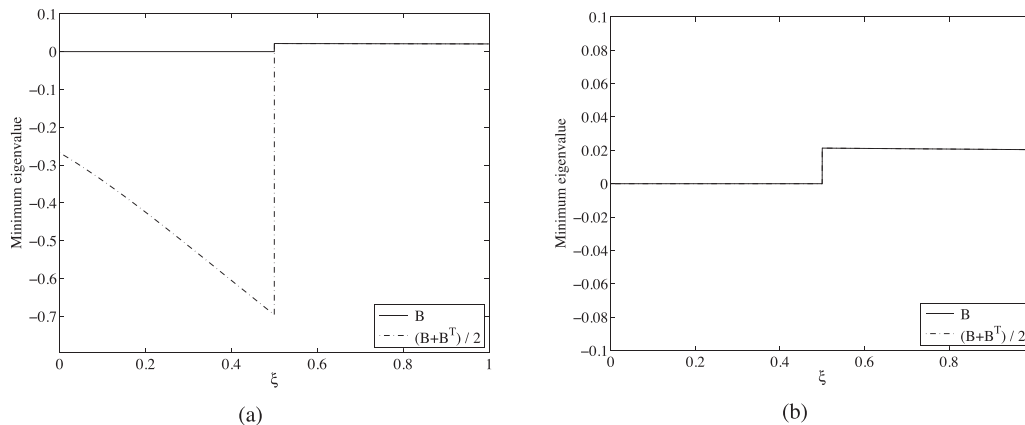


**Figure 3.** As Fig. 2, but with an increase of  $D^-$  to order  $M = 6$  near the Neumann boundary, again for (a)  $\xi_{0,p} = 0$  or (b)  $\xi_{0,p} = \frac{1}{2}$ . In the last panel, the curves lie on top of each other.

closer to the boundary than half a grid spacing were ignored in the discretization. In that paper, this was done to avoid a severe decrease of the maximum allowable time step. Here, we need it to have stability at all.

To control if points close to the boundary are ignored, we can define two parameters,  $\xi_{0,p}$  and  $\xi_{0,v}$ . The first parameter refers to the zero Dirichlet boundary condition of  $D^+$ , the second to the zero Neumann boundary condition of  $D^-$ . If the distance  $\xi \Delta x$  to the boundary of the last interior pressure point obeys  $\xi < \xi_{0,p}$ , that solution value is ignored in the spatial discretization. Instead, an extra interior point is adopted for the extrapolation operator, using the interior  $M/2$  points next to the point that is ignored. Likewise, velocity points with  $\xi < \xi_{0,v}$  can be ignored for the operator  $D^-$  at the Neumann boundary.

Numerical tests over the values of  $\xi \in [0, 1)$ , displayed in Fig. 2, show that we can have non-negative matrices for  $\xi_{0,p} = \frac{1}{2}$  and  $\xi_{0,v} = 0$  if  $M = 4$ . This means that pressure points closer than half a grid spacing to the boundary should be ignored, whereas for the velocity, we can just use the scheme as is.

We might increase the order of accuracy for the operator  $D^-$  that acts on the velocity by 2 near the boundary for reasons explained below. Figs 3(a) and (b) show the smallest eigenvalues if  $D^+$  has order  $M = M_d = 4$  and  $D^-$  has order  $M_n = 6$  at the boundary but order  $M = 4$  in the interior.

In all cases shown in Figs 2 and 3, the eigenvalues of  $B$  are non-negative. Those of  $B_{\text{sym}}$  are non-negative for  $\xi_{0,p} = \frac{1}{2}$  and  $\xi_{0,v} = 0$ . Similar results are found for orders  $M = 6$  and  $M = 8$  with  $\xi_{0,p} = \frac{1}{2}$  and  $\xi_{0,v} = 0$ .

For the implementation of this scheme, we used the extrapolation operators in Appendix A and also applied them to determine the value of the ignored interior point by interpolation.

### 2.4 Accuracy

To test the numerical accuracy of the proposed scheme, we first consider the function  $p(x) = \sin(4\pi x/x_{\text{max}})$  with  $x_{\text{max}} = 1 + (\xi - 1)\Delta x$ . We compare  $D^+ p(x_{p,j})$  to  $p_x = dp/dx$ , and  $D^- p_x(x_{v,j})$  to  $p_{xx} = d^2p/dx^2$ . Fig. 4 shows graphs of the maximum error in  $p_x$  and  $p_{xx}$  as a function of the spacing  $\Delta x$ , obtained for a fourth-order scheme ( $M = 4$ ). Note that for  $\xi_{0,p} = \frac{1}{2}$  and  $\xi_{0,v} = 0$ , the point too close the boundary, which is ignored by  $D^+$  and set to 0 by  $D^-$  for the stability plots, is excluded from the error measurements. In Figs 4(a) and (b), the observed exponent is 4.0 for  $p_x$ , but smaller for  $p_{xx}$ , decreasing to 3.0 in Fig. 4(a). To repair this behaviour, we can increase the order of  $D^-$  to  $M + 2$  at the boundary by increasing the order of the extrapolation operator and of the finite-difference weights at the boundary. Because the odd derivatives are set to zero during the extrapolation, we only have to include one additional interior point during the extrapolation. This means that for the pressure, we assume a function of the form  $p(x) = \sum_{k=1}^{M_d/2} a_{2k-1}(x - x_b)^{2k-1}$  near the boundary at  $x_b$ , whereas for the velocity or pressure derivative, we assume  $v(x) = \sum_{k=1}^{M_n/2} b_{2k-2}(x - x_b)^{2k-2}$ , with  $M_d = M$  and  $M_n = M + 2$  being even. To find  $p(x)$ , we need  $\frac{1}{2}M$  interior points, but for  $v(x)$ , we need one more:  $1 + \frac{1}{2}M$ .

With this increase of accuracy for  $D^-$ , the observed accuracy in Figs 4(c) and (d) is of order four. As mentioned before, the extrapolation operator for the pressure involves  $\frac{1}{2}M$  interior points closest to the boundary, but excludes points closer than  $\xi_{0,p}\Delta x$  for the pressure if  $\xi_{0,p} > 0$ . For the velocity, we do not have to exclude points near the boundary, which is expressed by the condition  $\xi_{0,v} = 0$ . However, the result after its numerical differentiation at the ignored pressure points is not included when measuring the errors for Fig. 4 and also earlier when computing the eigenvalues for Figs 2 and 3 if its distance to the boundary is smaller than half a grid spacing. This is required for stability in more than one dimension. In that case, interpolation on the resulting pressure field can be used to restore its value, as described in Section 3.3.

Results similar to Figs 2–4 are obtained for an eight-order scheme, with  $M = 8$ .

As a second set of tests, we consider the 1-D time-dependent problem of the wave equation with constant density and unit sound speed  $c = c_0 = 1$  on almost the unit interval  $[(1 - \xi)\Delta x, 1]$ . A pulse of the form  $w(x - ct)$  with  $w(x) = \cos^{12}[\pi(x - x_p)/w_p]$  for  $(x - x_p)/w_p < \frac{1}{2}$

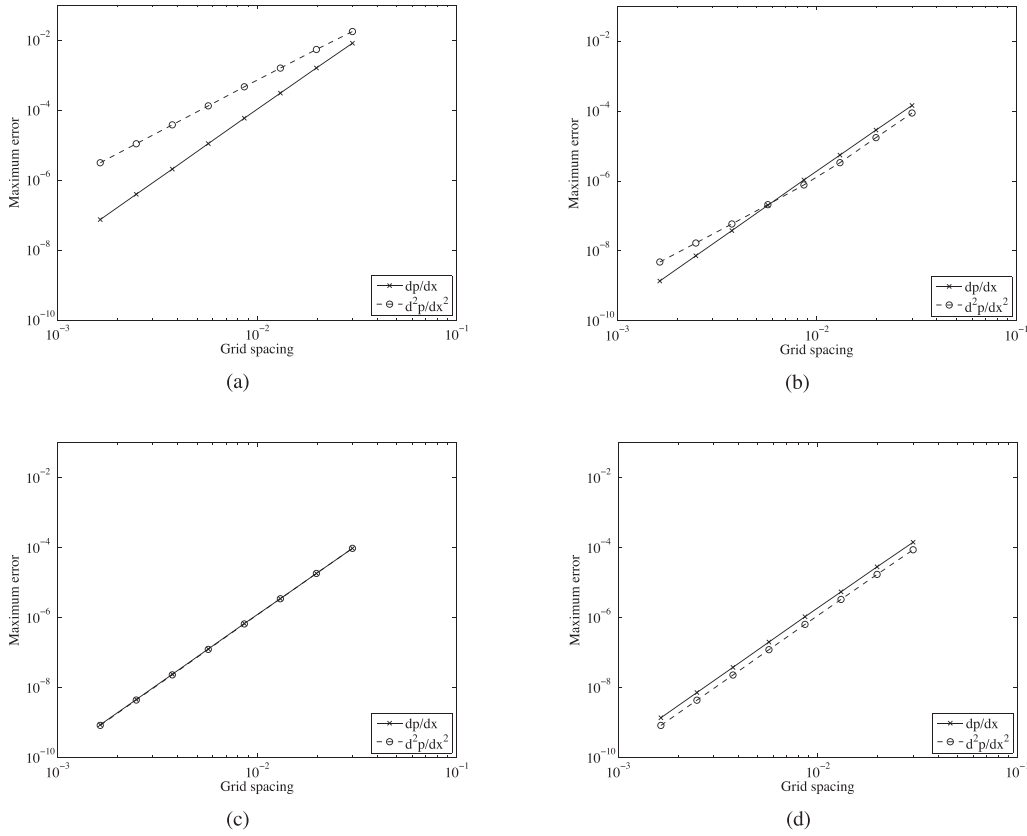


**Figure 4.** Accuracy test for 1-D differentiation with order  $M = 4$  in the interior, but near the boundary with order  $M_d$  for the pressure and order  $M_n$  for the velocity. Pressure values closer to the boundary than  $\xi_{0,p}\Delta x$  are ignored. The parameters are (a)  $\xi = 0.1$ ,  $\xi_{0,p} = 0$ ,  $M_d = M_n = 4$ ; (b)  $\xi = 0.9$ ,  $\xi_{0,p} = 0$ ,  $M_d = M_n = 4$ ; (c)  $\xi = 0.1$ ,  $\xi_{0,p} = \frac{1}{2}$ ,  $M_d = 4$ ,  $M_n = 6$ ; (d)  $\xi = 0.9$ ,  $\xi_{0,p} = \frac{1}{2}$ ,  $M_d = 4$ ,  $M_n = 6$ . The increase of  $M_n$  to 6 at the boundary restores the formal fourth-order accuracy when differentiating  $dp/dx$ .

and zero otherwise, centred at  $x_p = 0.5$  and with a width  $w_p = 0.8$ , travels to its starting point in a time  $T = 2[1 - (1 - \xi)\Delta x]/c_0$ . We apply a second-order leap-frog time stepping scheme on the initial data  $p(t = 0, x) = -c_0 w(x)$  and  $v(t = \frac{1}{2}\Delta t, x) = w(x - \frac{1}{2}\Delta t c_0)$ . A sufficiently small time-step will keep the temporal error small.

Fig. 5(a) shows the RMS errors as a function of grid spacing,  $\Delta x$ , for an eighth-order scheme ( $M = 8$ ). The domain ranged from  $(1 - \xi)\Delta x$  with  $\xi = 0.2$  to 1. The time step was set at 1 per cent of its maximum value. The observed order of accuracy is 5.2 rather than the expected 8. An increase of the order with 2 on the left boundary for the velocity extrapolation and the differentiation operator,  $D^-$ , produces the graphs in Fig. 5(b) with an estimated order of accuracy around 7.6.

Surprisingly, we observe a similar improvement in Fig. 5(c) without increasing the order but, instead, by dropping the point for the pressure if it is closer to the Dirichlet boundary than half a grid spacing. Dropping such points is not necessary for stability in 1D, but it is in 2D and 3D, as discussed in Section 2.3. These numerical experiments therefore suggest that we do not have to increase the order for  $D^-$  near the boundary and that for  $D^+$ , we should ignore the point closer than half a grid spacing to the boundary.

## 2.5 One-sided variant

The previous scheme imposes (anti)symmetry across the boundaries. This amounts to the requirement that all even derivatives of the pressure are zero on the boundary, including the zeroth derivative. Similarly, all odd derivatives of the velocity should be zero. This follows from the fact that, for instance,

$$\frac{1}{c^2} \frac{\partial^2 p}{\partial t^2} = \frac{\partial^2 p}{\partial x^2} \quad (10)$$

should hold on the boundary. If  $p = 0$  on the boundary, then  $\frac{\partial^2 p}{\partial t^2} = 0$  as well as all higher even time derivatives, implying that all even spatial derivatives should vanish on the boundary. If  $p = 0$  on the boundary for all time and the source sits at some distance from the boundary, then eq. (1) implies that  $\frac{\partial v}{\partial x} = 0$  on the boundary. Taking an odd number of spatial derivatives of  $\frac{\partial v}{\partial t} = \frac{\partial p}{\partial x}$  on the boundary implies that all odd spatial derivatives of  $v$  should vanish on the boundary since all even derivatives of  $p$  are zero.

In the 2-D case, we would like to use the same numerical 1-D boundary conditions. However, if the boundary-normal does not coincide with a coordinate direction, the above conditions on the derivatives along coordinate directions do not hold any more. The net effect will be a

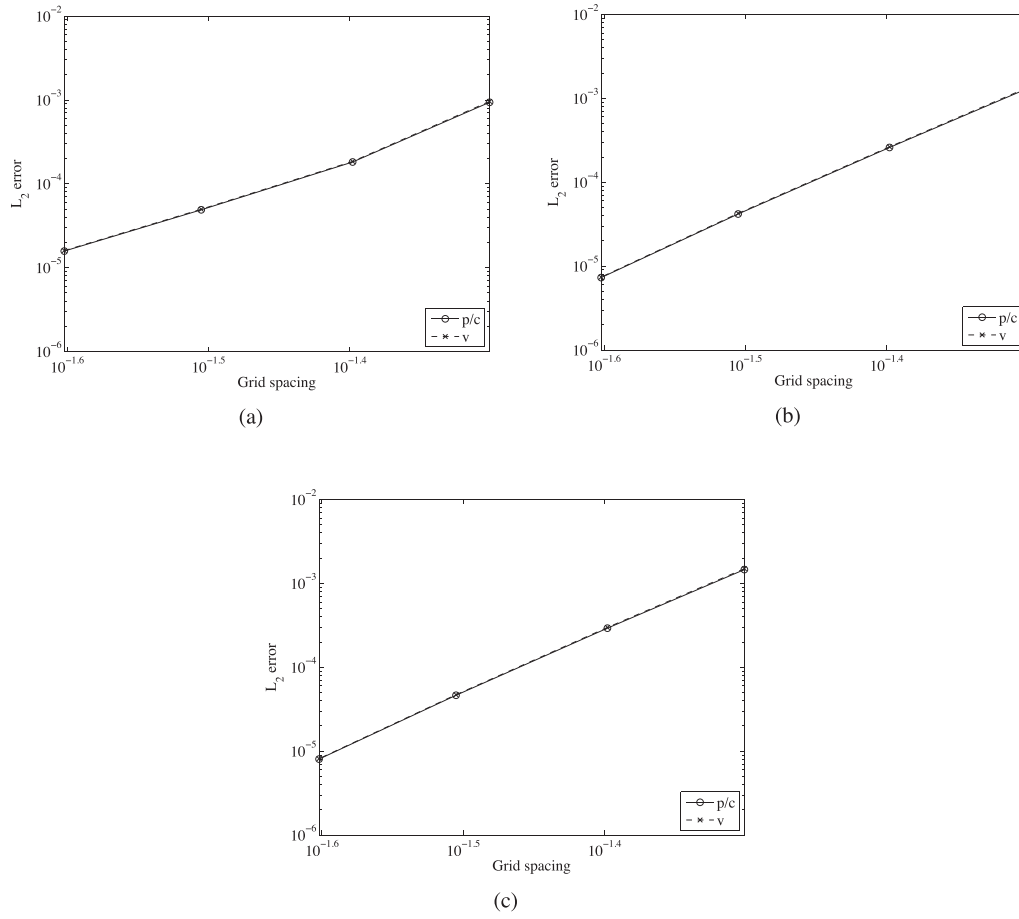


**Figure 5.** (a)  $L_2$ -error as a function of grid spacing,  $\Delta x$ , for a scheme of order  $M = 8$  with the left boundary at  $x = (1 - \xi)\Delta x$ ,  $\xi = 0.2$  and the right one at an unstaggered grid point at  $x = 1$  for a travelling pulse after it has returned to its original position. The observed order of accuracy is 5.1. (b) When the order of the operator  $D^-$  near the Neumann boundary condition, not coinciding with a grid point, is increased by 2, the observed order is 7.7, close to the expected 8. (c) The same happens to be the case without an increase of the order, but by ignoring the pressure point closest to the boundary if its distance to the boundary is less than half a spacing. In all cases, the results for  $p/c$  and  $v$  lie on top each other.

decrease of numerical accuracy near the boundary, although the results for the second-order formulation (Mulder 2017) suggest that the loss in accuracy may be acceptable in practice.

An alternative 1-D scheme, called the one-sided variant, can be considered that only imposes the zero boundary condition for the pressure and for the first derivate of the velocity. The former also holds in the 2-D case, the latter, however, generally not. Schemes of this type were studied by Mattsson & Nordström (2004) and are much harder to stabilize. We can apply a similar extrapolation scheme as before, but now,  $M - 1$  interior points are needed to complement the single boundary condition of either a zero function value or a zero first derivative. The resulting extrapolation operators are listed in Appendix B for orders  $M = 2$  to 6. Because only one boundary condition is available for the local Taylor series, more interior points are required, leading to longer stencils. In the numerical experiments described below, the order  $M = 8$  turned out to be unstable in 1D and 2D, whereas for  $M = 6$ , stability was observed in 1D but not in 2D. Also, we had to use the same approach as described in Section 2.3 for the other scheme, with  $\xi_{0,p} = \frac{1}{2}$ , to obtain stability in 2D. In view of these unattractive properties, no attempts were made to stabilize the scheme with weighted norms, along the lines of Mattsson & Nordström (2004). An alternative would be to lower the degree towards the boundary, but that approach has not been investigated.

### 3 2-D METHOD

#### 3.1 Interior

We will describe the method for the 2-D case. The generalization to 3-D is straightforward. The 2-D system of equations reads

$$\frac{1}{\rho c^2} \frac{\partial p}{\partial t} = \frac{\partial v_x}{\partial x} + \frac{\partial v_z}{\partial z} + f, \quad \rho \frac{\partial v_x}{\partial t} = \frac{\partial p}{\partial x}, \quad \rho \frac{\partial v_z}{\partial t} = \frac{\partial p}{\partial z}. \quad (11)$$



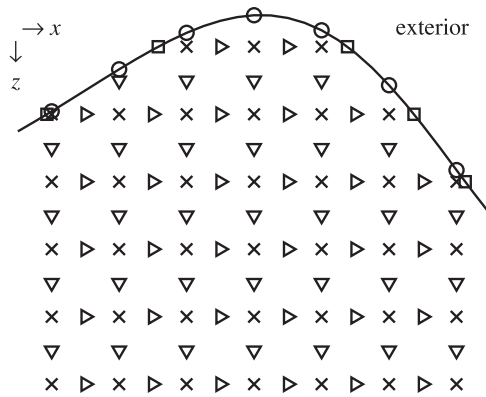


**Figure 6.** Staggered grid near the boundary. The crosses mark the positions of the pressure variables,  $p$ , the right-pointing triangles of the horizontal particle velocity,  $v_x$ , and the downward-pointing triangles of vertical velocity,  $v_z$ . The circles denote the boundary points involved in the vertical derivatives, the squares those required for the horizontal derivatives. Close to the surface, there may not be enough points for horizontal extrapolation with the desired polynomial degree.

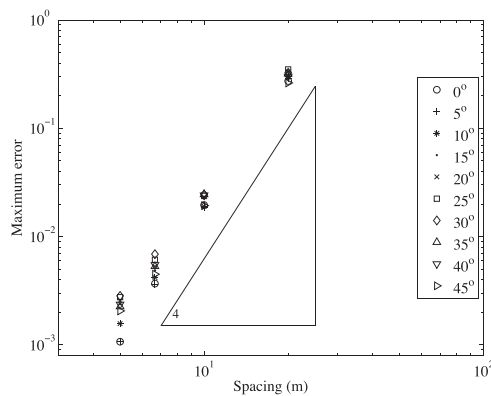


**Figure 7.** The maximum error in the pressure wavefield, divided by the amplitude of the latter, as a function of grid spacing,  $\Delta x$ , for a range of dip angles shows almost fourth-order convergence as indicated by the large triangle.

The solution values of the pressure,  $p$ , are placed on the unstaggered points of the modelling grid. The horizontal particle velocity,  $v_x$ , is staggered by half a spacing in the  $x$ -direction and the vertical velocity,  $v_z$ , by half a spacing in the  $z$ -direction. The grid is chosen such that the straight-line boundaries at  $x_{\min}$ ,  $x_{\max}$  and  $z_{\max}$  coincide with the unstaggered grid points. The same standard difference operators as in the 1-D case are applied in each coordinate direction.

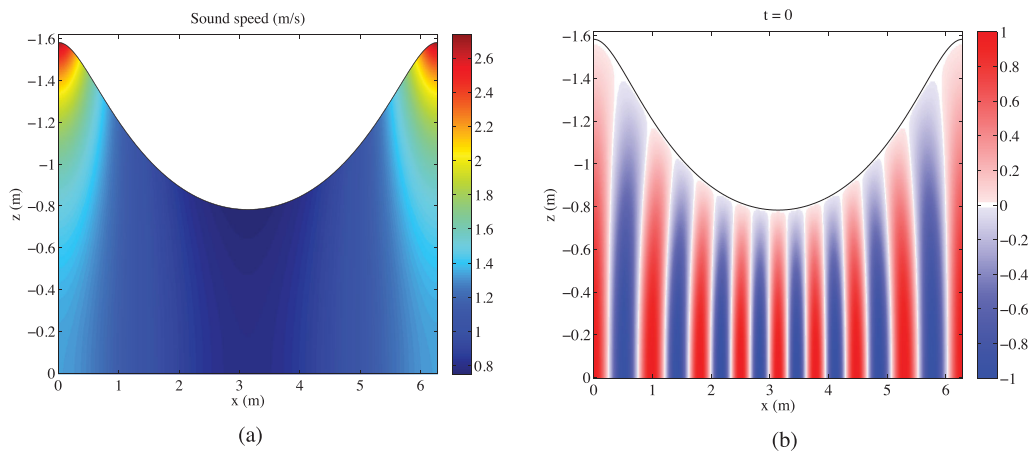


**Figure 8.** Sound speed (a) for the second test problem. The exact solution (b), shown at initial time, is periodic in the horizontal direction, has a zero normal derivative for the pressure at the bottom and a zero value of the pressure on the curved surface.

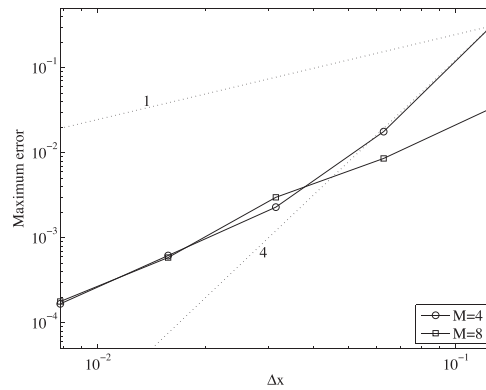


**Figure 9.** The maximum error in the pressure for the second test problem with a time step at half its maximum value for a discretization of order  $M = 4$  (circles) and order  $M = 8$  (squares) as a function of the horizontal grid spacing  $\Delta x$ . The dotted lines indicate the trends for first- and fourth-order convergence.

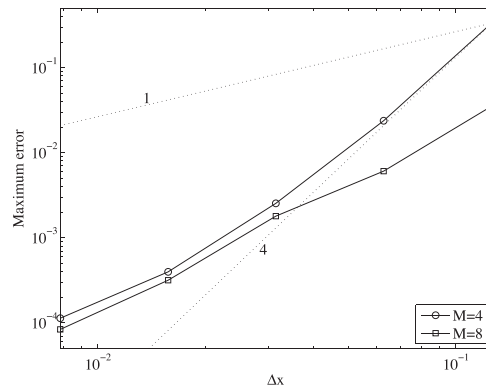


**Figure 10.** The maximum error in the pressure for the second test problem with a time step at 10 per cent of its maximum value for a discretization of order  $M = 4$  (circles) and order  $M = 8$  (squares) as a function of the horizontal grid spacing  $\Delta x$ . The dotted lines indicate the trends for first- and fourth-order convergence. Since the differences with Fig. 9 are small, the error must be dominated by the spatial discretization and boundary conditions.

### 3.2 Topography

In more than one space dimension, we can simply apply the 1-D scheme along grid lines, just as in (Mulder 2017) for the second-order formulation of the wave equation. As already remarked in the introduction, this will increase the error if the normal to the free surface does not coincide with a grid line.

Near the free-surface boundary, the interior difference scheme of eq. (4) can be replaced by a scheme that consists in its application to the interior points combined with the extrapolated values as defined in Appendix A for several orders. This is still a 1-D operation. Since it assumes more symmetry than is present when the boundary is not perfectly horizontal or vertical, an additional numerical error is incurred. It remains to be seen how that error affects the overall accuracy.

The extrapolated values are only used for the construction of the finite-difference operator in one direction and then discarded. They are not involved in the extrapolation in the other coordinate direction. Note that a different way of implementation is to directly store the action of the finite-difference operator on the extrapolated values, i.e. the modified difference operators, either obtained by the above construction or by evaluating explicit expressions for the combined effect of extrapolation and differentiation.

In the 2-D experiments, we have imposed periodic or zero Dirichlet or Neumann boundary conditions at the left and right and at the ‘bottom’, corresponding to the largest depth or  $z$ -value. These boundaries are assumed to be straight lines coinciding with the unstaggered grid points. For the smallest  $z$ -value, we assume topography, defined as a depth function of lateral position. The input is either a function  $z(x)$  or a set of points  $z_j = z(x_j)$ ,  $j = 1, \dots, N_{\text{topo}}$ . This set of points may have a smaller or larger spacing than the finite-difference grid. We therefore resample the topography by fitting a smooth cubic B-spline through the given  $z(x_j)$ . In the examples later on, we have somewhat arbitrarily resampled to a spline grid twice as coarse as the modelling grid.

For the test problems with an exact solution, the topography is known as a function  $(x(s), z(s))$ , where  $s$  parametrizes the boundary. Arc-length along the curve was chosen for the latter. Then,  $(x_j, z_j)$  on a grid 10 times finer than the modelling grid was evaluated from the analytical expression for the shape of the boundary. Next, piecewise cubic Hermite interpolation was applied to find a representation of  $(x(s), z(s))$ . The reason for choosing  $(x(s), z(s))$  instead of  $z(x)$  as a parametrization is the third test problem, which has a vertical boundary in one corner.

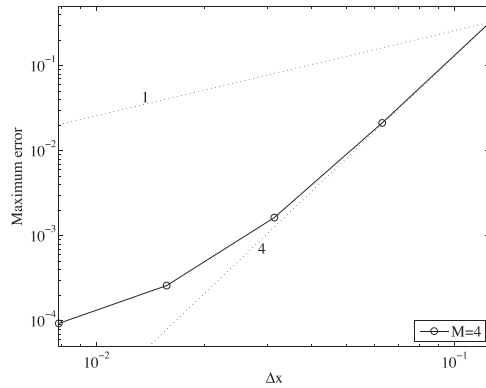


Figure 11. As Figs 9 and 10, but for the one-sided variant and order  $M = 4$  at 10 per cent of the maximum time step.

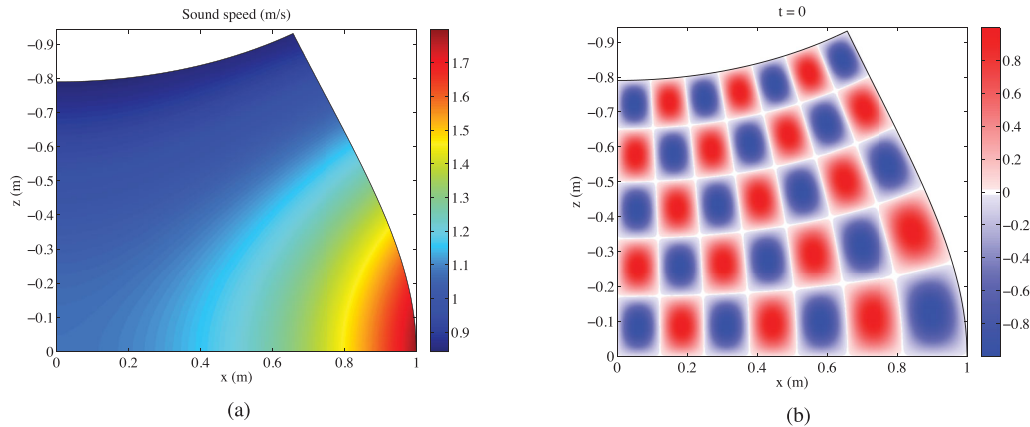


Figure 12. Sound speed (a) for the third test problem. The exact solution (b), here shown at zero time, represents a standing wave and has zero pressure on each boundary.

The extrapolation requires  $M/2$  points from the interior that may not always be available for the horizontal derivatives, as sketched in Fig. 6. If, for instance, a sixth-order scheme is to be used in the horizontal direction, 3 interior points are needed for extrapolation, whereas only two are available for  $v_x$  close to the summit. In that case, extrapolation is applied across each boundary in the following way. For the extrapolation,  $M$  conditions are required:

- (i) use  $M/2$  boundary conditions (all even or odd derivatives zeros) at the nearest boundary;
- (ii) interpolate through the available interior points;

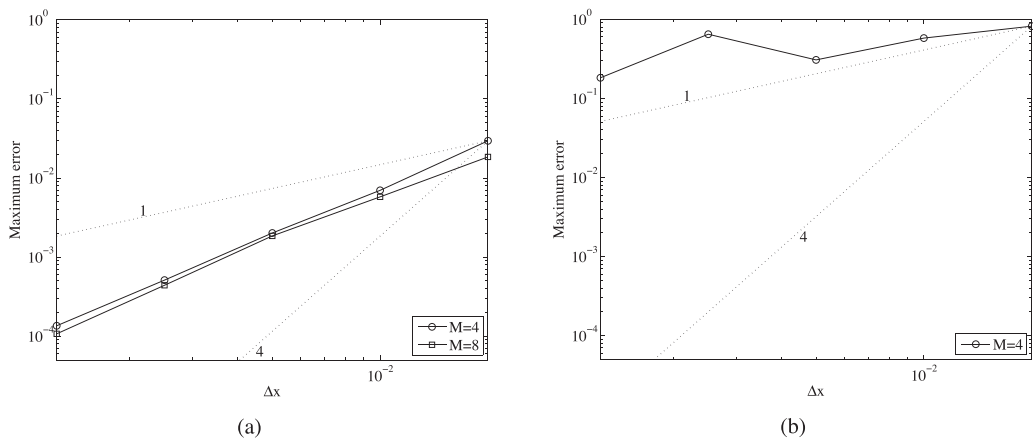
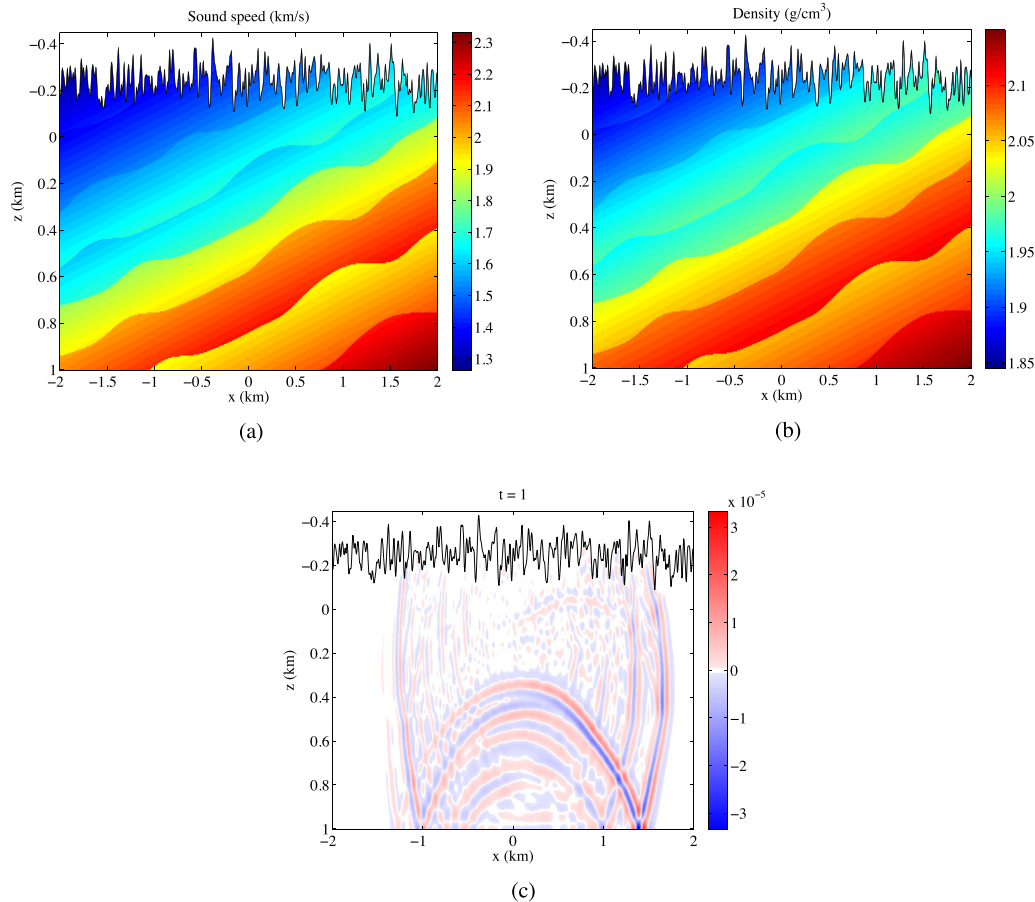


Figure 13. Maximum error in the pressure for the third test problem with a time step at half the maximum value for a discretization of order  $M = 4$  or 8 as a function of the horizontal grid spacing  $\Delta x$  (a). The dotted lines indicate first- and fourth-order convergence and the actual convergence is about second order for both. With pressure and velocities set to zero in the exterior and no special treatment of the free surface, worse than first-order error behaviour is observed (b).



**Figure 14.** Sound speed model (a) and density (b) for a model with a very rough topography as well as a snapshot (c) of the pressure wavefield after 1 s for a source at the centre, at a depth of 22 m below the surface. All boundaries are reflecting.

(iii) for the remaining unknowns, use the boundary conditions at the opposite boundary point, starting from the conditions on the lowest derivative.

In this way, an extrapolation operator to the left and one to the right can be constructed. The finite-difference weights are then applied to this operator to obtain the modified finite-difference scheme. Finding the intersection point of the vertical lines, on which the pressure or vertical displacement is defined, with the boundary is trivial for a spline of the form  $z(x)$ . For the horizontal lines, Newton's method can be used or, alternatively, an explicit evaluation of the cubic roots. In the case of a parametrization of the form  $(x(s), z(s))$ , one of those methods has to be used for both the horizontal and the vertical lines.

### 3.3 Reconstruction

In more than one space dimension, ignoring points closer to the zero Dirichlet boundary than half a spacing may cause problems in the other coordinate direction(s). An obvious solution is the reconstruction of the pressure at the ignored points with the same 1-D interpolating polynomial as used for the extrapolation beyond the Dirichlet boundary. Such a reconstruction can be performed after each temporal update of the pressure. In this way, the pressure is available during the next time step if it happens to be needed for another coordinate direction. An alternative is to let the time step update the pressure values, based on velocity derivatives and earlier pressure values, but this was observed to produce weak instabilities.

If a pressure point is closer than half a spacing to the boundary along coordinate lines in more than one direction, we can either perform 1-D interpolation based on the nearest boundary point or carry out multidimensional interpolation.

## 4 2-D RESULTS

We consider the same numerical test problems used before in the second-order formulation (Mulder 2017). The first three have an exact solution. They are followed by a problem with a very rough topography created with a random number generator and designed to push the method to its limits. The last two problems have a realistic topography but fantasy geology.

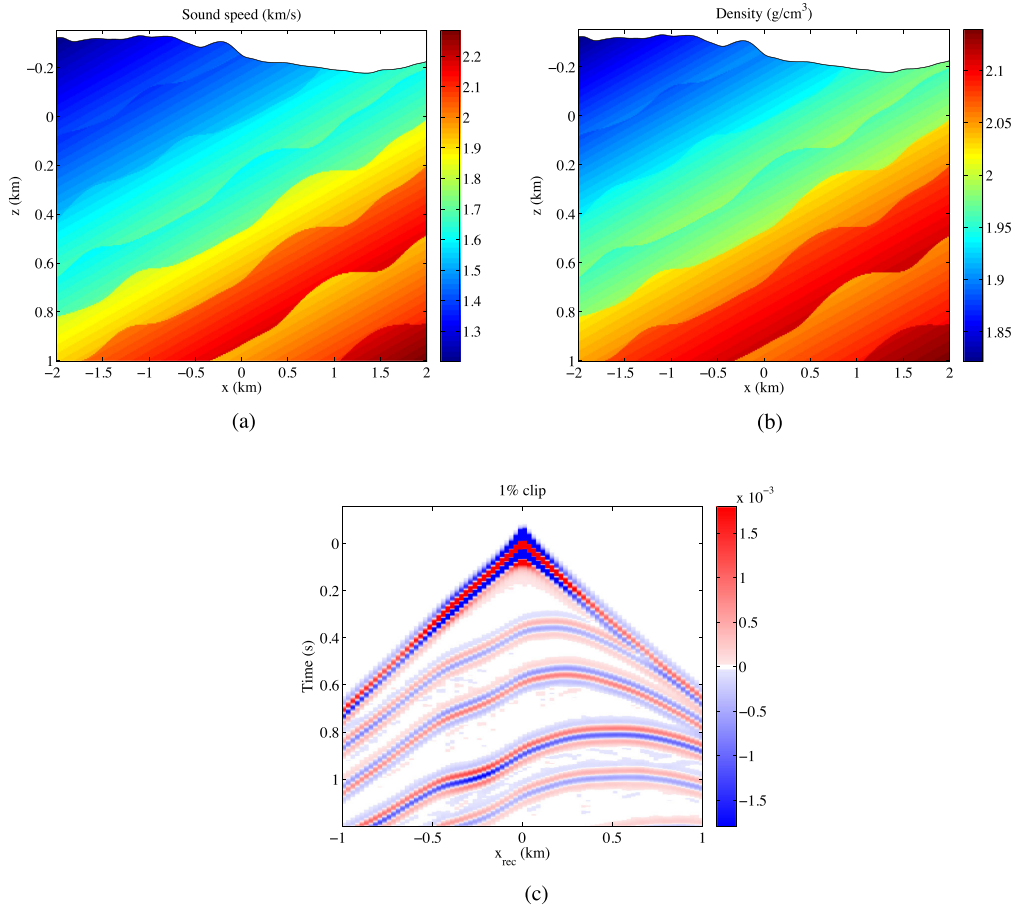


**Figure 15.** 2-D problem based on a cross-section through the topography of the Vaalserberg. The sound speed (a) and density model (b) are based on a geo-fantasy. The seismic traces (c) are dominated by the direct arrival and the stronger reflections.

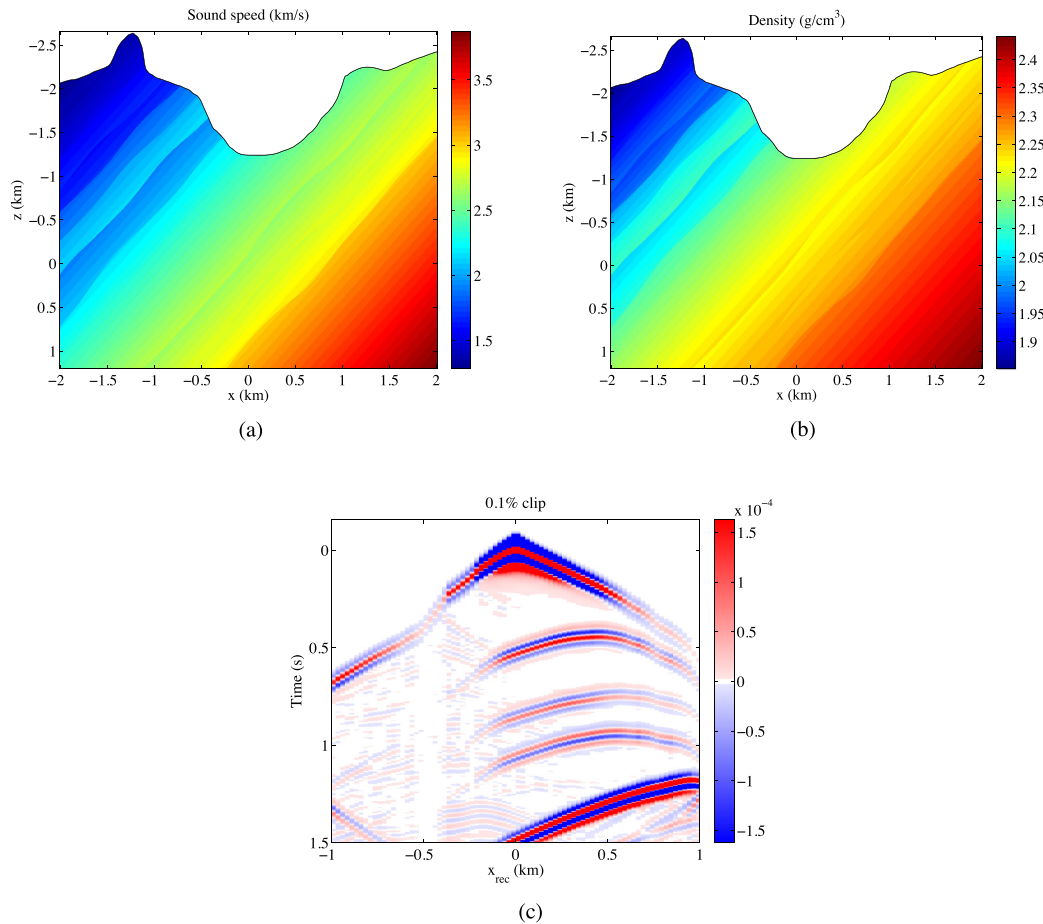
The first problem is a homogeneous half-space with a velocity of  $2 \text{ km s}^{-1}$  and a density of  $1 \text{ kg dm}^{-3}$ . The surface has a dip angle ranging from  $0^\circ$  to  $45^\circ$  at a  $5^\circ$  increment for the various tests. The source at  $60 \text{ m}$  distance to the surface has a wavelet  $w(t) = t[1 - (2t/T_w)^2]^7$  for  $|t| < T_w/2$  and zero otherwise, with a duration of  $T_w = 0.125 \text{ s}$ . It is the time integral of the one used in the second-order formulation (Mulder 2017). The simulations were started at  $-T_w/2$  with a time step at 10 per cent of the maximum value allowed for stability to keep the temporal error of the second-order time-stepping order sufficiently small. The error was measured at a time  $t = 0.4 \text{ s}$ . The solution consists of a direct wave that constitutes about half a circle together with its ghost. Fig. 7 plots the maximum error in the pressure wavefield, divided by the wavefield's amplitude, as a function of the grid spacing  $\Delta x$  for several dip angles. The observed convergence rate is close to fourth order at zero dip. At larger dips, where the approximation of symmetry or antisymmetry in the coordinate direction rather than in the normal direction of the free surface starts to play a role, the order of convergence becomes worse, closer to 3.5 on finer grids.

Fig. 8 shows the sound speed model for the second test problem, together with the pressure at initial time. The exact solution is a travelling wave, with a zero Dirichlet boundary condition at the surface (smallest  $z$ -values) and a zero Neumann boundary condition at the bottom. The left and right boundary conditions are periodic. The maximum error in the pressure after travelling around once on the periodic grid is shown in Fig. 9 for a sequence of grid spacings,  $\Delta x$  and a scheme of order 4 and 8, respectively. The time step was set at half its maximum value. For reference, the dotted lines show the convergence behaviour for orders 1 and 4.

In the case of an interior fourth-order spatial discretization ( $M = 4$ ), a fourth-order error in the pressure is observed on the coarser grids. On finer grids, the effects of the locally 1-D approximations in the boundary conditions start to appear and the convergence rate drops to about second-order. The same is true in the eighth-order case. Note that the error on the coarsest grid starts with a smaller value compared to the fourth-order case, making a scheme of order 8 still attractive for production runs.

To verify that the second-order time-stepping error does not dominate the results, we repeated the runs at 10 per cent of the maximum time step. Fig. 10 displays the resulting errors. As the difference with the earlier runs at half the maximum time step is small, we conclude that the error on finer grids must be dominated by the boundaries.

Fig. 11 displays the convergence behaviour for the one-sided variant with a fourth-order spatial discretization. The scheme appears to be slightly more accurate, compared to the result for order  $M = 4$  in Fig. 10. Unfortunately, it turned out to be unstable for orders  $M = 6$  and  $M = 8$ , and is therefore less attractive.



**Figure 16.** Synthetic sound speed (a) and (b) density model for a line with its topography take from Half Dome, together with seismic traces (c).

The third test problem with an exact solution is a standing wave. The same parameters were used as in the second-order case (Mulder 2017). Fig. 12 shows the sound speed model and the initial pressure distribution. A zero-pressure boundary condition is imposed all around. The maximum errors for a series of runs on different grids are plotted in Fig. 13. Given the long wavelengths of the solution, relative to the computational grids used in the experiments, we expect the boundary errors to dominate in this example. Fig. 13(a) displays a convergence rate around second-order, both for the locally 1-D schemes of order 4 and 8.

The next test problem was designed to push the method to its limits and has the topography shown in Fig. 14(a). A shot placed at 22 m below the surface generates the wavefield displayed in Fig. 14(b). The wavelet was the time integral of a 12-Hz Ricker. Our method appears to be robust enough to handle this test problem.

Finally, we consider a pair of tests based on actual topography. Fig. 15 shows a cross-section through the Vaalserberg, the highest mountain in The Netherlands. The sound speed is a geo-fantasy, as is the density model. For simplicity, zero Neumann boundary conditions are imposed for the pressure at the sides and the bottom, whereas zero pressure is imposed on the surface boundary. The source sits at the centre, 13 m below the surface. Receivers are placed at a depth of 5 m below the surface in a split-spread acquisition up to a maximum offset of 1 km and record the pressure. The source wavelet was, again, the time integral of a 12-Hz Ricker. The result is qualitatively the same as that obtained with the second-order constant-density formulation in (Mulder 2017).

Fig. 16(a) shows a similar example with the topography of Half Dome and a fantasy sound speed and density model. The shot was located 12 m below the surface. The wavelet was the same as in the previous example. Receivers were again placed 5 m below the surface. The amplitude variations along the surface are more pronounced than in the previous example.

## 5 3-D RESULTS

Figs 17 and 18 show a comparison of our finite-difference scheme based on 1-D field extensions with a continuous mass-lumped finite-element approach (CML-FEM, Zhebel *et al.* 2014) for a rough 3-D topography somewhere in south-eastern Europe. Both methods were run with a 5-Hz Ricker wavelet and a constant sound speed of  $2500 \text{ m s}^{-1}$ . For this comparison, we have used a buried source at the centre and at a depth of about 970 m below the surface.

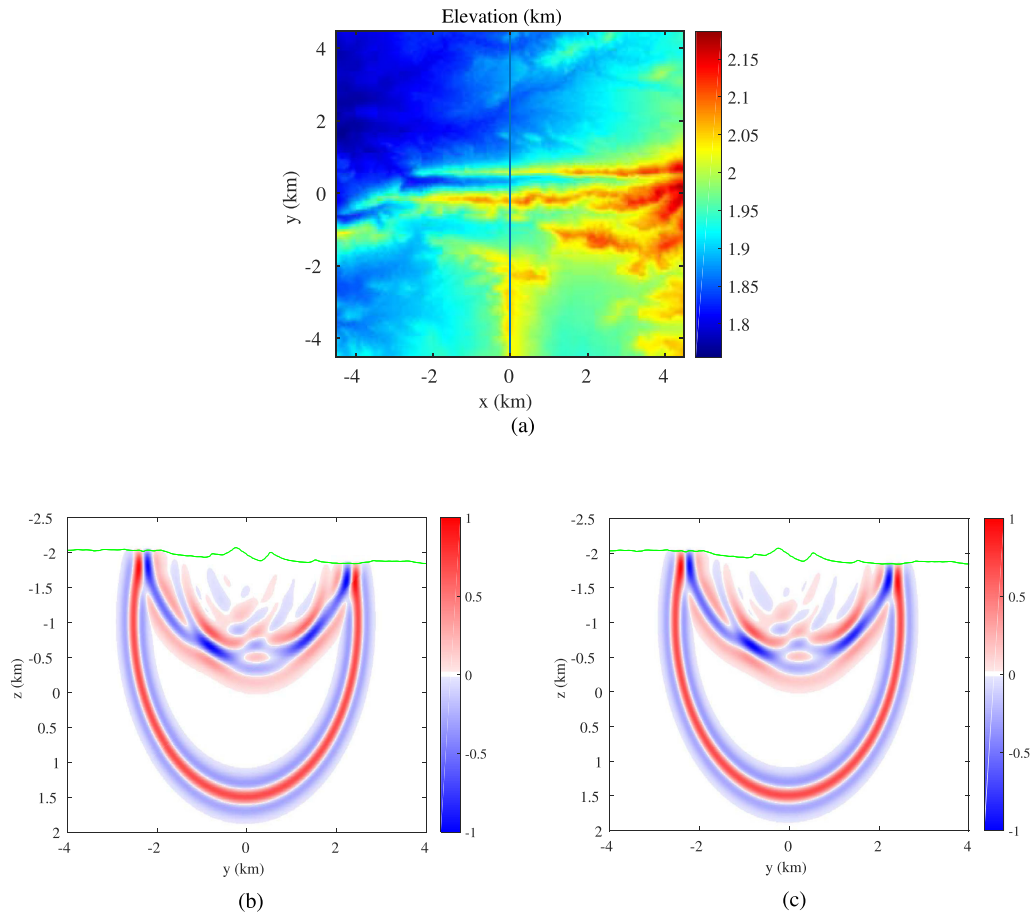


**Figure 17.** (a) Elevation map of a  $9 \times 9$  km area in south-eastern Europe. Elevations range from 1750 to 2200 m. (b) Pressure snapshot after 1 s of propagation with the finite-difference method. (c) Pressure snapshot after 1 s of propagation with the finite-element method.

The 3-D finite-difference simulation was performed using an implementation of the approach in an FWI production system, taking numerical parameters for regular production settings. The results were obtained with an eighth-order spatial discretization at five grid points per wavelength. Both the snapshots in Figs 17(b) and (c) as well as the normalized shot panels in Figs 18(a) and (b) show a close agreement between the finite-difference and finite-element results. Their differences, shown in Fig. 18(c), have a maximum error of 0.04. Results at 4 points per wavelength are very similar with slightly larger a maximum error of 0.05.

## 6 CONCLUSIONS

Stability and accuracy of a modified finite-difference scheme that can handle topography in the first-order formulation of the acoustic wave equation has been studied by a series of 1-D, 2-D and 3-D tests. The boundary conditions consist in imposing antisymmetry for the pressure and symmetry for each particle velocity component on the boundary in its corresponding coordinate direction. Because the coordinate direction and corresponding velocity components rather than the normal direction and normal velocity component are chosen, an additional numerical error is incurred, on top of the errors caused by the interior spatial discretization and the time stepping scheme.

The modification of the finite-difference scheme near the boundary results in an instability in more than one space dimension, which can be removed by ignoring pressure values closer to the boundary than half a grid spacing. Because these values may still be needed for derivatives in another coordinate direction, reconstruction by polynomial interpolation is applied.

In a simple 2-D test with a dipped flat surface, the observed convergence rate for the spatial error is around order four, although the maximum error loses about half an order for larger dips. In a 2-D test with a variable velocity, a curved interface, and a solution that has a long wavelength compared to the grid spacing of the computational grid, the boundary error dominates and reduces the overall spatial accuracy to order two. To put this into perspective, we note that a high-order finite-difference scheme also reduces to second-order accuracy in the interior when differencing across discontinuities in the velocity or density, because the pressure is continuous but not differentiable over there.

3-D examples exhibit acceptable accuracy for our boundary scheme when using typical production-run parameters.

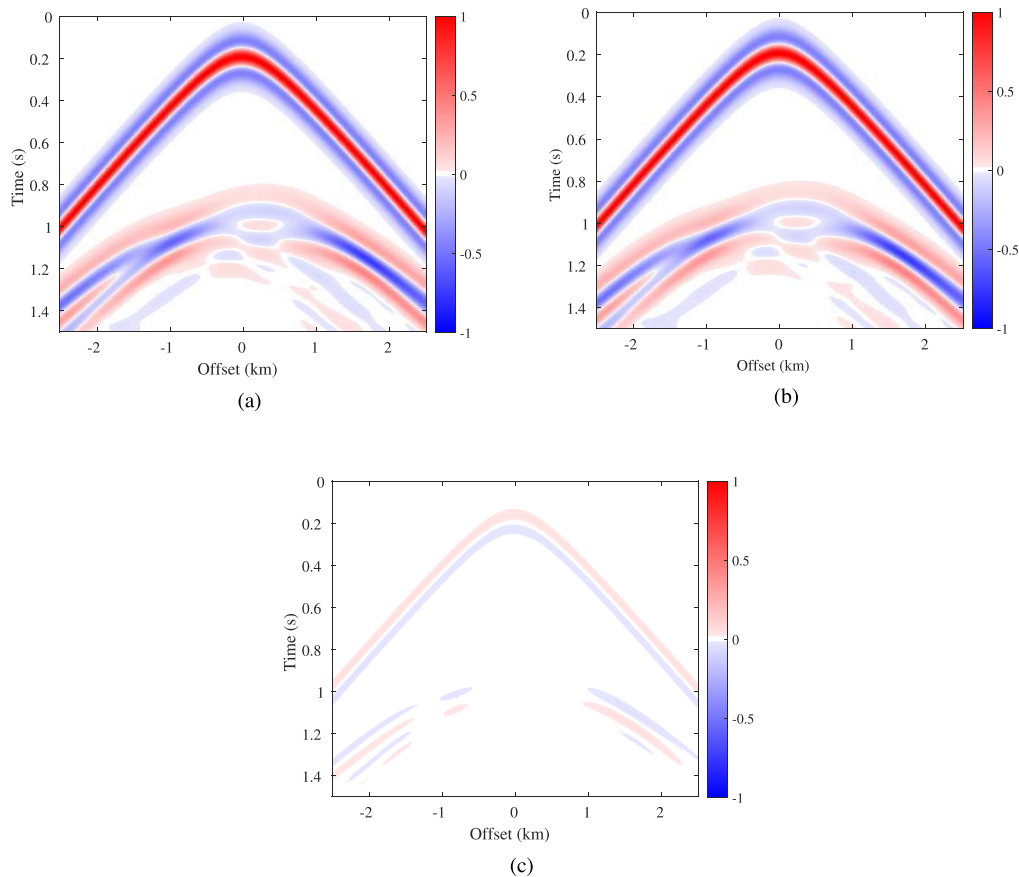


**Figure 18.** (a) Normalized shot panel for a receiver line 500 m below the source along the central vertical line in the elevation map of Fig. 17, obtained with the finite difference method. (b) Same shot panel obtained with the finite-element method. (c) Difference of the shot panels in (a) and (b).

## REFERENCES

- AlMuhaidib, A.M., Fehler, M., Toksöz, M.N. & Zhang, Y., 2011. Finite difference elastic wave modeling including surface topography, in *SEG Technical Program Expanded Abstracts 2011*, pp. 2941–2946.
- Bartel, L.C., Symons, N.P. & Aldridge, D.F., 2000. Graded boundary simulation of air/Earth interfaces in finite-difference elastic wave modeling, in *SEG Technical Program Expanded Abstracts 2000*, pp. 2444–2447.
- Bécache, E., Joly, P. & Tsogka, C., 2000. An analysis of new mixed finite elements for the approximation of wave propagation problems, *SIAM J. Numer. Anal.*, **37**(4), 1053–1084.
- Benjema, M., Glinsky-Olivier, N., Cruz-Atienza, V.M., Virieux, J. & Piperno, S., 2007. Dynamic non-planar crack rupture by a finite volume method, *Geophys. J. Int.*, **171**(1), 271–285.
- Bohlen, T. & Saenger, E.H., 2006. Accuracy of heterogeneous staggered-grid finite-difference modeling of Rayleigh waves, *Geophysics*, **71**(4), 109–115.
- Boore, D.M., 1972. Finite difference methods for seismic wave propagation in heterogeneous materials, in *Seismology: Surface Waves and Earth Oscillations*, vol. 11 of *Methods in Computational Physics: Advances in Research and Applications*, pp. 1–37, ed. Bold, B.A., Elsevier.
- Carpenter, M.H., Nordström, J. & Gottlieb, D., 1999. A stable and conservative interface treatment of arbitrary spatial accuracy, *J. Comput. Phys.*, **148**(2), 341–365.
- Charney, J.G., Fjörtoft, R. & von Neumann, J., 1950. Numerical integration of the barotropic vorticity equation, *Tellus*, **2**, 237–254.
- Chin-Joe-Kong, M.J.S., Mulder, W.A. & van Veldhuizen, M., 1999. Higher-order triangular and tetrahedral finite elements with mass lumping for solving the wave equation, *J. Eng. Math.*, **35**, 405–426.
- Cohen, G., Joly, P., Roberts, J.E. & Tordjman, N., 2001. Higher order triangular finite elements with mass lumping for the wave equation, *SIAM J. Numer. Anal.*, **38**(6), 2047–2078.
- De Basabe, J.D. & Sen, M.K., 2007. Grid dispersion and stability criteria of some common finite-element methods for acoustic and elastic wave equations, *Geophysics*, **62**(6), T81–T95.
- De la Puente, J., Ferrer, M., Hanzich, M., Castillo, J.E. & Cela, J.M., 2014. Mimetic seismic wave modeling including topography on deformed staggered grids, *Geophysics*, **79**, T125–T141.
- Dormy, E. & Tarantola, A., 1995. Numerical simulation of elastic wave propagation using a finite volume method, *J. geophys. Res.*, **100**(B2), 2123–2133.
- Dumbser, M., Käser, M. & de la Puente, J., 2007. Arbitrary high-order finite volume schemes for seismic wave propagation on unstructured meshes in 2D and 3D, *Geophys. J. Int.*, **171**(2), 665–694.
- Etienne, V., Chaljub, E., Virieux, J. & Glinsky, N., 2010. An hp-adaptive discontinuous Galerkin finite-element method for 3-D elastic wave modelling, *Geophys. J. Int.*, **183**(2), 941–962.
- Fornberg, B., 2010. A finite difference method for free boundary problems, *J. Comput. Appl. Math.*, **233**(11), 2831–2840.
- Gao, L., Brossier, R., Pajot, B., Tago, J. & Virieux, J., 2015. An immersed free-surface boundary treatment for seismic wave simulation, *Geophysics*, **80**(5), T193–T209.
- Grote, M.J., Schneebeli, A. & Schötzau, D., 2006. Discontinuous Galerkin finite element method for the wave equation, *SIAM J. Numer. Anal.*, **44**(6), 2408–2431.
- Haney, M.M., 2007. Generalization of von Neumann analysis for a model of two discrete half-spaces: the acoustic case, *Geophysics*, **72**(5), SM35–SM46.



- Hestholm, S. & Ruud, B., 1998. 3-D finite-difference elastic wave modeling including surface topography, *Geophysics*, **63**, 613–622.
- Hestholm, S. & Ruud, B., 2002. 3D free-boundary conditions for coordinate-transform finite-difference seismic modelling, *Geophys. Prospect.*, **50**(5), 463–474.
- Hu, W., 2015. IBFD for seismic wave modeling—regular grid method handling arbitrary topography, in *SEG Technical Program Expanded Abstracts 2015*, pp. 3544–3548.
- Joly, P., 2003. Variational methods for time-dependent wave propagation problems, in *Topics in Computational Wave Propagation*, vol. 31 of *Lecture Notes in Computational Science and Engineering*, pp. 201–264, eds Ainsworth, M., Davies, P., Duncan, D., Rynne, B. & Martin, P., Springer.
- Komatitsch, D. & Vilotte, J., 1998. The spectral element method: an efficient tool to simulate the seismic response of 2-D and 3-D geological structures, *Bull. seism. Soc. Am.*, **88**, 368–392.
- Lipnikov, K., Manzini, G. & Shashkov, M., 2014. Mimetic finite difference method, *J. Comput. Phys.*, **257**, 1163–1227.
- Lombard, B., Piraux, J., Gélis, C. & Virieux, J., 2008. Free and smooth boundaries in 2-D finite-difference schemes for transient elastic waves, *Geophys. J. Int.*, **172**(1), 252–261.
- Mattsson, K. & Nordström, J., 2004. Summation by parts operators for finite difference approximations of second derivatives, *J. Comput. Phys.*, **199**(2), 503–540.
- Mattsson, K. & Nordström, J., 2006. High order finite difference methods for wave propagation in discontinuous media, *J. Comput. Phys.*, **220**(1), 249–269.
- Mattsson, K., Almqvist, M. & Carpenter, M.H., 2014. Optimal diagonal-norm SBP operators, *J. Comput. Phys.*, **264**, 91–111.
- Minisini, S., Zhebel, E., Kononov, A. & Mulder, W.A., 2013. Local time stepping with the discontinuous Galerkin method for wave propagation in 3D heterogeneous media, *Geophysics*, **78**(3), T67–T77.
- Mittel, R., 2002. Free-surface boundary conditions for elastic staggered-grid modeling schemes, *Geophysics*, **67**(5), 1616–1623.
- Moczo, P., Robertsson, J.O. & Eisner, L., 2007. The finite-difference time-domain method for modeling of seismic wave propagation, in *Advances in Wave Propagation in Heterogeneous Earth*, vol. 48 of *Advances in Geophysics*, pp. 421–516, eds Wu, R.-S., Maupin, V. & Dmowska, R., Elsevier.
- Moczo, P., Kristek, J., Galis, M., Chaljub, E. & Etienne, V., 2011. 3-D finite-difference, finite-element, discontinuous-Galerkin and spectral-element schemes analysed for their accuracy with respect to *P*-wave to *S*-wave speed ratio, *Geophys. J. Int.*, **187**(3), 1645–1667.
- Modave, A., St-Cyr, A., Mulder, W.A. & Warburton, T., 2015. A nodal discontinuous Galerkin method for reverse-time migration on GPU clusters, *Geophys. J. Int.*, **203**(2), 1419–1435.
- Mulder, W.A., 1996. A comparison between higher-order finite elements and finite differences for solving the wave equation, in *Proceedings of the Second ECCOMAS Conference on Numerical Methods in Engineering*, Paris, Sept. 9–13, 1996, pp. 344–350, John Wiley & Sons, Chichester.
- Mulder, W.A., 2017. A simple finite-difference scheme for handling topography with the second-order wave equation, *Geophysics*, **82**(3), T111–T120.
- Mulder, W.A. & Shamasundar, R., 2016. Performance of continuous mass-lumped tetrahedral elements for elastic wave propagation with and without global assembly, *Geophys. J. Int.*, **207**(1), 414–421.
- Nesemann, L., 2014. Numerical acoustic-elastic coupling and curved boundaries for RTM, in *76th EAGE Conference & Exhibition*, Amsterdam, Netherlands, Extended Abstracts, We G105 03.
- Pelties, C., Hermann, M.K.V. & Castro, C.E., 2010. Regular versus irregular meshing for complicated models and their effect on synthetic seismograms, *Geophys. J. Int.*, **183**(2), 1031–1051.
- Petersson, N.A. & Sjögreen, B., 2015. Wave propagation in anisotropic elastic materials and curvilinear coordinates using a summation-by-parts finite difference method, *J. Comput. Phys.*, **299**, 820–841.
- Piriaux, J. & Lombard, B., 2001. A new interface method for hyperbolic problems with discontinuous coefficients: one-dimensional acoustic example, *J. Comput. Phys.*, **168**(1), 227–248.
- Rivière, B. & Wheeler, M., 2003. Discontinuous finite element methods for acoustic and elastic wave problems, *Contemp. Math.*, **329**, 271–282.
- Robertsson, J.O., 1996. A numerical free-surface condition for elastic/viscoelastic finite-difference modeling in the presence of topography, *Geophysics*, **61**(6), 1921–1934.
- Schultz, C.A., 1997. A density-tapering approach for modeling the seismic response of free-surface topography, *Geophys. Res. Lett.*, **24**(22), 2809–2812.
- Seo, J.H. & Mittal, R., 2011. A high-order immersed boundary method for acoustic wave scattering and low-mach number flow-induced sound in complex geometries, *J. Comput. Phys.*, **230**, 1000–1019.
- Seriani, G., Priolo, E., Carcione, J. & Padovani, E., 1992. High-order spectral element method for elastic wave modeling, *SEG Technical Program Expanded Abstracts*, **11**, 1285–1288.
- Shortley, G.H. & Weller, R., 1938. Numerical solution of Laplace's equation, *J. Appl. Phys.*, **9**(5), 334–344.
- Solano, C.A.P., Donno, D. & Chauris, H., 2016. Finite-difference strategy for elastic wave modelling on curved staggered grids, *Comput. Geosci.*, **20**(1), 245–264.
- Strand, B., 1994. Summation by parts for finite difference approximations for  $d/dx$ , *J. Comput. Phys.*, **110**(1), 47–67.
- Tessmer, E. & Kosloff, D., 1994. 3-D elastic modeling with surface topography by a Chebychev spectral method, *Geophysics*, **59**(3), 464–473.
- Zeng, C., Xia, J., Miller, R.D. & Tsoflias, G.P., 2012. An improved vacuum formulation for 2D finite-difference modeling of Rayleigh waves including surface topography and internal discontinuities, *Geophysics*, **77**, T1–T9.
- Zhang, J. & Gao, H., 2009. Elastic wave modelling in 3-D fractured media: an explicit approach, *Geophys. J. Int.*, **177**(3), 1233–1241.
- Zhang, J. & Liu, T., 1999. P-SV-wave propagation in heterogeneous media: grid method, *Geophys. J. Int.*, **136**(2), 431–438.
- Zhang, W. & Chen, X., 2006. Traction image method for irregular free surface boundaries in finite difference seismic wave simulation, *Geophys. J. Int.*, **167**(1), 337–353.
- Zhang, D., Schuster, G. & Zhan, G., 2013. Multi-source least-squares reverse time migration with topography, in *SEG Technical Program Expanded Abstracts*, pp. 3736–3740.
- Zhebel, E., Minisini, S., Kononov, A. & Mulder, W.A., 2011. Solving the 3D acoustic wave equation with higher-order mass-lumped tetrahedral finite elements, in *73rd EAGE Conference & Exhibition incorporating SPE EUROPEC*, Vienna, Austria, Extended Abstracts, A010.
- Zhebel, E., Minisini, S., Kononov, A. & Mulder, W.A., 2014. A comparison of continuous mass-lumped finite elements with finite differences for 3-D wave propagation, *Geophys. Prospect.*, **62**(5), 1111–1125.

## APPENDIX A: BOUNDARY EXTRAPOLATION OPERATORS

For the lowest order,  $M = 2$ , extrapolation of  $p$ , where  $j$  is distance of the target point to the last interior point and  $\xi$  is the distance of the boundary to the last interior point, obeys  $E^d(\xi, j) = ((\xi - j)/\xi)$ . For  $v$ , we have  $E^n(\xi, j) = (1)$ .

If  $\xi < \frac{1}{2}$ , shown in Fig. 1(a), no extrapolation is needed for  $D^+$ . Otherwise, its last rows and columns become

$$D^+ = \frac{1}{\Delta x} \begin{pmatrix} \ddots & & \vdots & \vdots & \vdots & \vdots \\ \dots & -1 & 1 & 0 & 0 & \\ \dots & & 0 & -1 & 1 & 0 \\ \dots & & & 0 & -\frac{1}{\xi} & 0 \end{pmatrix}. \quad (\text{A1})$$

Because  $\xi \geq \frac{1}{2}$ , the entry with  $-1/\xi$  will not cause problems. In the second-order formulation, the fact that  $\xi$  could approach zero forced the time step bound to zero and for that reason, points close to the boundary had to be ignored. Here, this does not seem to be necessary in the 1-D case, but it is in a 2-D or 3-D setting, as argued in Section 2.3. The operator  $D^-$ , acting on the points shown as dots in Fig. 1, does not require extrapolation for  $\xi \geq \frac{1}{2}$  whereas for  $\xi < \frac{1}{2}$  and  $M = 2$ , it produces zero in the last interior point, marked by a cross in Fig. 1(a).

For  $M = 4$ , extrapolation for  $p$  is given by

$$E^d(\xi, j) = \frac{\xi - j}{1 + 2\xi} \left( \frac{j(j - 2\xi)}{1 + \xi}, \frac{(1 + j)(1 + 2\xi - j)}{\xi} \right), \quad (\text{A2a})$$

with special cases

$$E^d(j, j) = (0, 0), \quad E^d(\xi, 1) = \frac{\xi - 1}{1 + 2\xi} \left( \frac{1 - 2\xi}{1 + \xi}, 4 \right). \quad (\text{A2b})$$

For a pressure grid with index  $N_x - 1$  for the last interior points, this leads to

$$\begin{pmatrix} p_{N_x} \\ p_{N_x + 1} \end{pmatrix} = E \begin{pmatrix} p_{N_x} - 2 \\ p_{N_x} - 1 \end{pmatrix}, \quad E_{j,k} = E_k^d(\xi, j). \quad (\text{A3})$$

Extrapolation for  $v$  is given by

$$E^n(\xi, j) = \left( \frac{j(j - 2\xi)}{1 + 2\xi}, \frac{(1 + j)(1 + 2\xi - j)}{1 + 2\xi} \right). \quad (\text{A4})$$

For  $M = 6$  and  $p$ ,

$$E^d(\xi, j) = \frac{j - \xi}{1 + \xi} \left( -\frac{j(j + 1)(j - 2\xi - 1)(j - 2\xi)}{4(\xi + 2)(2\xi + 3)}, \frac{j(j + 2)(j - 2\xi)(j - 2\xi - 2)}{(2\xi + 1)(2\xi + 3)}, -\frac{(j + 1)(j + 2)(j - 2\xi - 1)(j - 2\xi - 2)}{4\xi(2\xi + 1)} \right), \quad (\text{A5})$$

with special cases  $\xi = \frac{1}{2}, j = 1$ , or  $j = 2$ . For  $v$ ,

$$E^n(\xi, j) = \left( \frac{j(j + 1)(j - 2\xi - 1)(j - 2\xi)}{4(\xi + 1)(2\xi + 3)}, -\frac{j(j + 2)(j - 2\xi - 2)(j - 2\xi)}{(2\xi + 1)(2\xi + 3)}, \frac{(j + 1)(j + 2)(j - 2\xi - 2)(j - 2\xi - 1)}{4(\xi + 1)(2\xi + 1)} \right). \quad (\text{A6})$$

Finally, for  $M = 8$  and  $p$ ,

$$E^d(\xi, j) = \frac{j - \xi}{3 + 2\xi} \left( -\frac{j(j + 1)(j + 2)(j - 2\xi - 2)(j - 2\xi - 1)(j - 2\xi)}{12(\xi + 2)(\xi + 3)(2\xi + 5)}, \frac{j(j + 1)(j + 3)(j - 2\xi - 3)(j - 2\xi - 1)(j - 2\xi)}{4(\xi + 1)(\xi + 2)(2\xi + 5)}, \right. \\ \left. -\frac{j(j + 2)(j + 3)(j - 2\xi - 3)(j - 2\xi - 2)(j - 2\xi)}{4(\xi + 1)(\xi + 2)(2\xi + 1)}, \frac{(j + 1)(j + 2)(j + 3)(j - 2\xi - 3)(j - 2\xi - 2)(j - 2\xi - 1)}{12\xi(\xi + 1)(2\xi + 1)} \right), \quad (\text{A7})$$

whereas for  $v$ ,

$$E^n(\xi, j) = \left( \frac{j(j + 1)(j + 2)(j - 2\xi - 2)(j - 2\xi - 1)(j - 2\xi)}{12(\xi + 2)(2\xi + 3)(2\xi + 5)}, -\frac{j(j + 1)(j + 3)(j - 2\xi - 3)(j - 2\xi - 1)(j - 2\xi)}{4(\xi + 1)(2\xi + 3)(2\xi + 5)}, \right. \\ \left. \frac{j(j + 2)(j + 3)(j - 2\xi - 3)(j - 2\xi - 2)(j - 2\xi)}{4(\xi + 2)(2\xi + 1)(2\xi + 3)}, -\frac{(j + 1)(j + 2)(j + 3)(j - 2\xi - 3)(j - 2\xi - 2)(j - 2\xi - 1)}{12(\xi + 1)(2\xi + 1)(2\xi + 3)} \right). \quad (\text{A8})$$

In all cases, the components obey

$$(\xi - j)E_k^n(\xi, j) = (\xi - k + \frac{1}{2}M)E_k^d(\xi, j), \quad k = 1, \dots, \frac{1}{2}M. \quad (\text{A9})$$

Note that the last element of  $E^d(\xi, j)$  always contains a factor  $1/\xi$ , which does not cause divergence as we always have  $\xi \geq \frac{1}{2}$  on a staggered grid.

**APPENDIX B: BOUNDARY EXTRAPOLATION OPERATORS FOR VARIANT 2**

For  $M = 2$ , we have the same operators as in the previous case. For  $M = 4$  and extrapolation of  $p$ ,

$$E^d(\xi, j) = \frac{\xi - j}{2} \left( \frac{j(j+1)}{\xi+2}, -\frac{2j(j+2)}{\xi+1}, \frac{(j+1)(j+2)}{\xi} \right), \tag{B1}$$

whereas for  $v$ ,

$$E^n(\xi, j) = \frac{1}{2(2+3\xi(2+\xi))} (-j(j+1)[j(1+2\xi) - \xi(2+3\xi)], 2(j+2)[j(2+2\xi) - \xi(4+3\xi)], \\ -(j+1)(j+2)[j(3+2\xi) - 2 - 3\xi(2+\xi)]). \tag{B2}$$

For  $M = 6$ ,

$$E^d(\xi, j) = \frac{\xi - j}{24} \left( \frac{j(j+1)(j+2)(j+3)}{\xi+4}, -\frac{4j(j+1)(j+2)(j+4)}{\xi+3}, \frac{6j(j+1)(j+3)(j+4)}{\xi+2}, \\ -\frac{4j(j+2)(j+3)(j+4)}{\xi+1}, \frac{(j+1)(j+2)(j+3)(j+4)}{\xi} \right), \tag{B3}$$

and

$$E^n(\xi, j) = \frac{1}{24(24+5\xi(4+\xi)(5+\xi(4+\xi)))} (-j(j+1)(j+2)(j+3)(2j(2\xi+3)(\xi(\xi+3)+1) - \xi(\xi(\xi(5\xi+24)+33)+12)), \\ 4j(j+1)(j+2)(j+4)(j(\xi(\xi(4\xi+21)+28)+8) - \xi(5\xi+8)(\xi(\xi+4)+2)), \\ -6j(j+1)(j+3)(j+4)(2j(\xi+2)(2\xi(\xi+4)+3) - \xi(\xi(\xi(5\xi+32)+57)+24)), \\ 4j(j+2)(j+3)(j+4)(j(\xi(\xi(4\xi+27)+52)+24) - \xi(\xi(\xi(5\xi+36)+78)+48)), \\ -(j+1)(j+2)(j+3)(j+4)(2j(2\xi+5)(\xi(\xi+5)+5) - 5\xi(\xi+4)(\xi(\xi+4)+5) - 24)). \tag{B4}$$

The scheme for order  $M = 8$  is unstable in 1D.